Weak-Beam Dark-Field Microscopy

26

CHAPTER PREVIEW

The term "weak-beam microscopy" refers to the formation of a diffraction-contrast image in either BF or DF. The DF approach has been more widely used, in part because it can be understood using quite simple physical models. It also gives stronger contrast; we see white lines on a dark gray background. This chapter will be concerned only with the DF approach. Historically, the weak-beam dark-field (WBDF, often abbreviated to WB) method became important because, under certain special diffraction conditions, dislocations can be imaged as narrow lines which are approximately 1.5 nm wide. Equally important is the fact that the positions of these lines are well defined with respect to the dislocation cores; they are also relatively insensitive to both the foil thickness and the position of the dislocations in the specimen. The technique is particularly useful if you are studying dissociated dislocations where pairs of partial dislocations may only be ~4 nm apart and yet this separation greatly affects the properties of the material.

We first choose a particular **g** and bring this onto the optic axis as if intending to form a regular on-axis DF image. We then tilt the specimen to make $\mathbf{s}_g$ large and examine the DF image using reflection **g**. If a defect is present, the diffracting planes may be bent locally back into the Bragg-diffracting orientation to give more intensity in the DF image. The problem is that, as we increase $\mathbf{s}_g$, the average intensity decreases as $1/s^2$; in the DP the beam appears as a weak spot, hence the name. When $\mathbf{s}_g$ is large, the coupling between **g** and the di-

D. B. Williams et al., *Transmission Electron Microscopy*

rect beam becomes small and the diffracted beam is said to be "kinematically diffracted." So, this chapter is where we will discuss the "kinematical approximation."

- You will sometimes see reference to the **g**(3**g**) WB condition. Beware! Sometimes you don't need to be this weak; sometimes this is not weak enough.
- It is often not the fact that **s** is large that is important; what is important is that ξ_{eff} is small.

This chapter is unusual in that it deals with a special imaging technique, rather than a concept or theory. Also, WBDF is only really useful when the specimen is not perfect, i.e., when you are interested in defects in the specimen or small changes in thickness. Therefore, you can skip this chapter if crystal-lattice defects are not relevant to your microscopy study. If you are interested in defects, you will find that this chapter really covers much more than WB microscopy. For example, we will use concepts developed for diffracted beams and carefully set the excitation error, $\mathbf{s}_g$, by referring to the Kikuchi-line pattern. In Section 26.9 we will discuss some of the ways that new developments in TEM design are changing the way we do WB microscopy and how we interpret the images.

Weak-Beam Dark-Field Microscopy

26

26.1. INTENSITY IN WBDF IMAGES

We showed in Chapter 11 that, in a two-beam situation, the intensity of the diffracted beam **g** in a perfect crystal can be written as

$$\left|\phi_g\right|^2 = \left(\frac{\pi t}{\xi_g}\right)^2 \cdot \frac{\sin^2(\pi t s_{eff})}{(\pi t s_{eff})^2} \qquad [26.1]$$

Remember that when we derived this expression we assumed that only two beams, O and G, are important. We will consider complications which arise when more beams are present in Section 26.9. The important variables in equation 26.1 are the thickness, t, and the effective excitation error, s_{eff}, which is given by

$$s_{eff} = \sqrt{s^2 + \frac{1}{\xi_g^{\,2}}} \qquad [26.2]$$

In the WB technique we increase s to about 0.2 nm^{-1} so as to increase s_{eff}. (In most WB papers you will see this value as 2×10^{-2} $Å^{-1}$.) This large value of s means that s_{eff}, and therefore the intensity, I_g, become independent of ξ_g except as a scaling factor for t (in the prefactor in equation 26.1). The actual value of **s** can be set by carefully positioning the Kikuchi lines for the systematic row of reflections which includes **g**. You can best appreciate this effect by calculating a range of values for **s**. Remember when doing this that you must specify **g** and the kV because, as we saw in Chapter 11, ξ_g varies with both the reflection used to form the WB image and the energy of the electrons

$$\xi_{eff} = \frac{\xi_g}{\sqrt{w^2 + 1}} \qquad [26.3]$$

A comment on equation 26.2: if $s \gg \xi_g^{-2}$ then $s \approx s_{eff}$, so that equation 26.2 becomes what is known as the "kinematical equation"; the kinematical equation cannot be applied for small **s** unless the thickness, t, is also very small.

Practical Considerations: As the value of s_{eff} increases, equation 26.1 shows that the intensity of the G beam decreases very rapidly. The result is that the exposure time needed to record the image on a photographic film also rapidly increases and has, in the past, been the factor which limited the usefulness of the technique. Although manufacturers may guarantee a drift rate of less than 0.5 nm per minute for new machines, values of six times this rate are common on many older instruments. The problem can be partly overcome by using photographic film with a fast emulsion or by modifying photographic processing conditions. In either case, the grainy appearance of the photographic emulsion would be increased. The problem of drift can, in principle, be overcome by using a video system to record the image and capturing frames from the video. You could then reduce the noise by frame averaging, particularly if you can take account of any drift. The causes of drift (specimen and thermal effects) and their correction or minimization are discussed in Chapter 8, but it is worth reminding you that change in the temperature of the water in the objective lens is a major cause of drift. Although WBDF imaging may aim for 0.5-nm resolution rather than 0.2 nm in HRTEM, exposure times are often 10 times greater for WBDF than HRTEM, so drift may be even more important.

26.2. SETTING s_g USING THE KIKUCHI PATTERN

Since the contrast in the WB image is so dependent on the value of $\mathbf{s}_g$ we need a method for determining $\mathbf{s}_g$. We draw a line through the **g**-systematic row and let the Ewald sphere cut through this line at $n\mathbf{g}$, where n is not an integer. Figure 26.1 illustrates this situation. How can we "see" what the value of n is? Of course we can't, since we are looking ap-

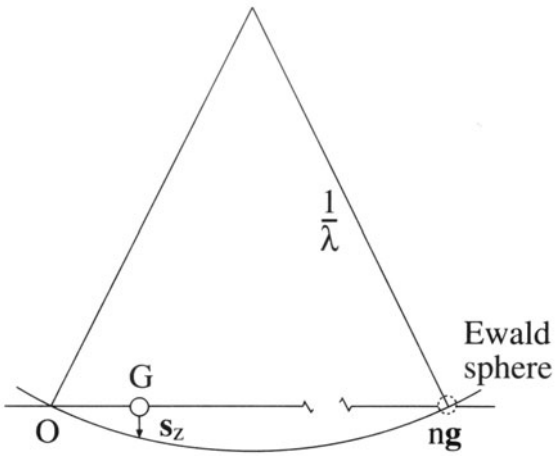

Figure 26.1. The Ewald sphere construction showing the diffraction conditions used to obtain weak-beam images. The sphere cuts the row of systematic reflections at "*n***g**" where *n* is not necessarily an integer.

proximately normal to the ZOLZ. We can't just judge *n* by looking at the intensities of the spots except in special circumstances.

The solution to the problem can be appreciated by looking at the Kikuchi pattern shown in Figure 26.2. When **g** is exactly at the Bragg condition, the **g** Kikuchi line passes through the **g** reflection; when 3**g** is exactly satisfied, the 3**g** Kikuchi line passes through the 3**g** reflection. We might guess that *n* is ~3.2 in Figure 26.2, but we don't have a 3.2**g** Kikuchi line; we have to deduce this value of *n* from the position of the 3**g** Kikuchi line. Remember (from Chapter 19) that when the 3**g** Kikuchi line passes through 3.5**g** on the **g**-systematic row, the 4**g** Kikuchi line and the Ewald sphere pass through the 4**g** reflection, as shown in Figure 26.3. Therefore, when the Ewald sphere passes through 3.2**g**, the 3**g** Kikuchi line will pass through 3.1**g**; we can express this simple geometric result as

$$n = 2m - N \qquad [26.4]$$

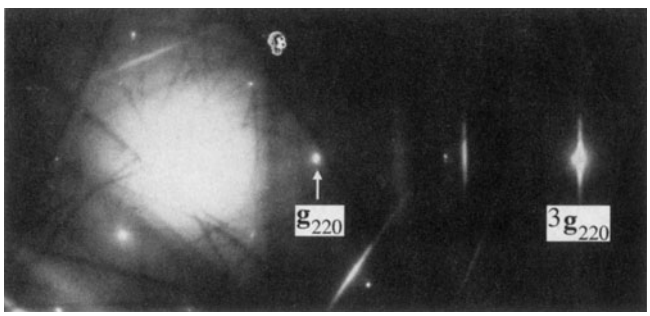

Figure 26.2. A DP obtained when the specimen is tilted to a suitable orientation for WB microscopy. Here **g** is a 220 reflection and 3**g** is strong.

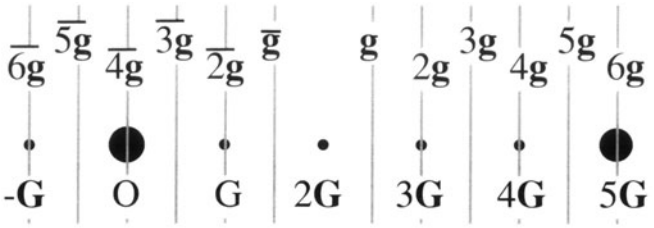

Figure 26.3. A schematic diagram showing the positions of the Kikuchi lines for the systematic row of reflections when 4**g** is excited.

where *N***g** refers to the Kikuchi line closest to *n***g** (*N* is an integer) and *m***g** is the location of the Kikuchi line as we measure it. In the example above, we can choose *N* to be 3 so that, if *m* is 3.1, then *n* is 3.2; if, instead, we choose *N* to be 4, then *m* is 3.6 (because we measure the position of the 4**g** Kikuchi line) and *n* is still 3.2. Having determined *n* we need to estimate **s**. This we do using the expression

$$\mathbf{s} = \frac{1}{2}(n-1)|\mathbf{g}|^2\lambda \qquad [26.5]$$

which you can derive from Figure 26.4 using the intersecting chord theorem ($ab = cd$) and the fact that $1/\lambda$ is much larger than **s**.

You can immediately appreciate some important results from this expression:

- Setting $n = -1$ gives the same value of **s** as for $n = 3$, but the sign is reversed.
- The magnitude of **s** is more strongly dependent on |**g**| than on λ, but it depends on *both*.
- The specific nature of the material enters through **g**, the microscope affects **s** through λ. Here we recommend that you use a spreadsheet to calculate different values of **s** as you vary **g** or λ. A selection of these for Cu and Si is given in Table 26.1.

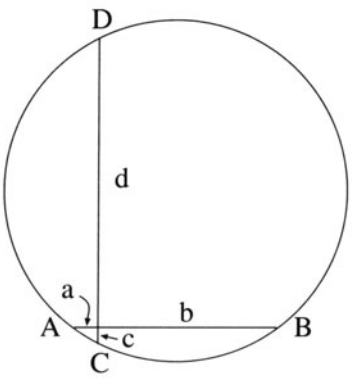

Figure 26.4. The intersecting chord construction used to deduce the value of $\mathbf{s}_g$: we approximate *d* to $2/\lambda$, *c* is **s**, *a* is |**g**|, and *b* is $(n\text{-}1)|\mathbf{g}|$.

Table 26.1. Values of S (Å^{-1}) for Various kV[a]

Si	Cu	Accelerating Voltage			
n_{Si}	n_{Cu}	100 kV	200 kV	300 kV	400 kV
4.9	2.8	0.020	0.014	0.011	0.009
6.9	3.6	0.030	0.020	0.016	0.013
8.5	4.3	0.038	0.025	0.020	0.017
9.9	4.9	0.044	0.030	0.024	0.020

[a]For Cu, a = 0.3607 nm; for Si, a = 0.534 nm. The values of n are accurate to better than 0.1. In both cases the calculation is for **g** = 220.

As an exercise, you can use equations 26.2 and 26.5 to calculate s_{eff} with ξ_g = 42 nm for the 220 reflection in Cu at 100 kV. You can then see when s_{eff} becomes "independent" of ξ_g. Next, repeat the exercise with other values of λ or for other reflections and materials.

One point you should bear in mind is that none of the above discussion requires a particular value for **s**, and yet you will often read that **s** must be ≥ 0.2 nm^{-1} for a WB image. This value of **s** is recommended when you are studying defects quantitatively, because computer calculations show that the position of the image can then be directly related to the position of the defect. You will find that smaller values of **s** will often give you WB images which contain the information you want and you can more easily see and record the image!

26.3. HOW TO DO WBDF

The nature of the WB image imposes a restriction on the maximum specimen thickness which you can use because the visibility of such images decreases as the thickness increases (due to a corresponding increase in inelastic scattering). However, the orientation of the specimen is accurately set by reference to the Kikuchi lines observed in the DP (Chapter 19), and these are not visible in specimens which are too thin. Therefore, your specimen thickness must be greater than a certain minimum value. Also, if the observations you made on certain defects, in particular dislocation ribbons and nodes, are to be interpreted as representative of the bulk and not influenced by the surface of the foil, then again your foil must not be too thin. You can generally satisfy these requirements by selecting defects for detailed study which, in the case of Cu and its alloys, lie in areas which are about 70 nm thick.

Due to the very low intensity of the WB images, exposure times required are typically on the order of 4 to 30 seconds using Kodak SO-163 film. The main factor limiting the exposure time is the inherent instability of any specimen stage. To minimize the exposure time, you can usually use a highly convergent (or divergent) beam, contrary to the assumption implicit in the simple theory. The effect of this convergence is that oscillations in image intensity and position, which result from variations in depth and thickness parameters, are diminished.

Step-by-step: We'll go through how to set up the **g**(3.1**g**) diffraction mode condition since this is widely used in practice. Actually, we generally refer to it as "**g**(3**g**) with $\mathbf{s}_{3g}$ positive" because we guess the value of n by estimating m. This condition ensures that the 3**g** reflection is not satisfied and also that you can use the BF **0**(**g**) image, with $\mathbf{s}_g$ slightly positive, to locate the defect and to focus your image. The first two steps are illustrated in Figure 26.5, relating what happens in the Ewald sphere model with what you see happening to the Kikuchi lines.

- Orient the specimen in BF so that **g** is excited and $\mathbf{s}_g$ is just greater than zero. Make sure that no other reflections are excited.
- Use the DF beam-deflecting coils to bring the reflection **g** on to the optic axis. Use the binoculars because **g** becomes very weak; underfocus the beam before you use the high-resolution screen.
- Insert the objective aperture. In BF, check that the aperture is centered, then switch to DF and check that the spot G is centered in the aperture.
- Fine-tune your conditions, looking at the DP with G centered.
- Go to imaging mode; you now have a WB image with the required **g**(3.1**g**) condition.

Since you have inserted a small objective aperture, you should now check the objective astigmatism. We use a small objective aperture so as to remove inelastic scattering; remember that this aperture will then limit our potential resolution. If you focus the beam, you may change the position of the beam and probably the astigmatism! Remove the objective aperture and check that no other reflections are strongly excited when you are in DF. Then repeat the process starting at the third step (insert the objective aperture).

After finely focusing the image, record it together with its SAD pattern.

If you're not sure why this "trick" for setting the **g**(3.1**g**) condition works, go back to Chapter 19 and draw the systematic row and the corresponding Kikuchi lines. Then move the spots, while keeping the crystal, and thus the Kikuchi lines, fixed. You may see the diffraction condition **g**($\bar{\mathbf{g}}$) used. This was the original condition suggested by Cockayne *et al.* (1969); it does give you the same values of **s** as the **g**(3.1**g**) condition, but the interband scattering processes are different and it is not so convenient to change from BF to WBDF. However, you may find variations on

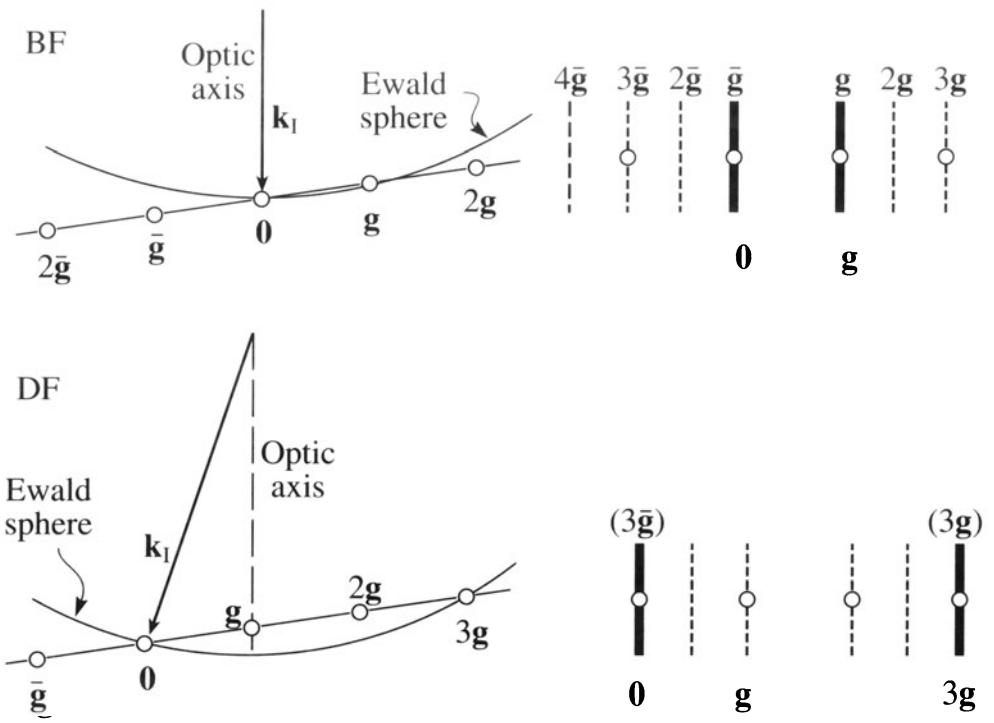

Figure 26.5. Relationship between the orientation of the Ewald sphere and the position of the Kikuchi lines for the **0**(**g**) (upper) and **g**(3**g**) (lower) diffraction conditions. The two pairs of diagrams are related by tilting the beam; the specimen has not tilted so the position of the Kikuchi lines is unchanged.

this condition useful when you need to use a **g**(*n***g**) condition with a large value of *n*.

Weak-beam microscopy becomes much easier when you are comfortable with using the TV camera. Just being able to see whether the image is moving due to specimen drift can save boxes of photographic film. As we mentioned earlier, you could use frame averaging to reduce the noise. However, you will realize that the extra magnification from the video system tends to limit the area which can be viewed, so that film is still preferred for most images. You will find that 30 k× magnification on the plate is a good compromise; without video, you will use 50-60 k× to allow you to focus with the binoculars.

26.4. THICKNESS FRINGES IN WEAK-BEAM IMAGES

Thickness fringes in WB images are just like thickness fringes in strong-beam images but the effective extinction distance, ξ_{eff}, is much smaller. From equation 26.1 we can see that the intensity minimum occurs at thicknesses of $\mathcal{N}(s_{eff}^{-1})$ with maxima at $(\mathcal{N}+ {}^1/_2)(s_{eff}^{-1})$. The effective extinction distance for s = 0.2 nm^{-1} is 5 nm; this value is rather sensitive to the precise value of s so that the fringes will change if the foil bends. Using WB images we can form a rather detailed contour map of the specimen, but you must remember that both surfaces may be inclined to the beam, as shown in Figure 26.6.

The thickness effect is illustrated in Figure 26.7. These images were recorded with s = 0.2 nm^{-1}. The MgO specimen has been heat-treated so that there are large regions where the surface is atomically flat on both sides.

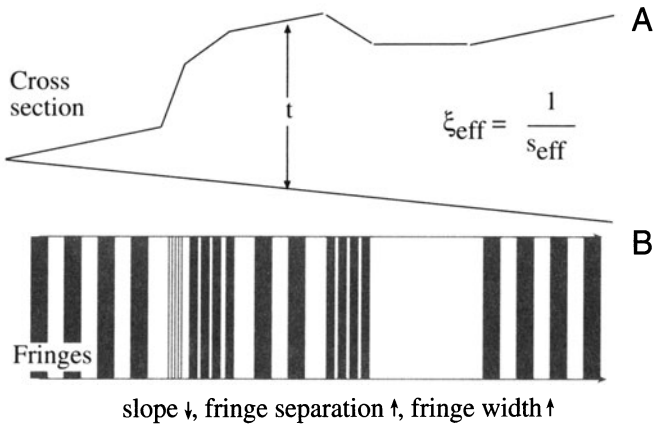

Figure 26.6. (A) In WB imaging, the thickness periodicity depends on the effective extinction distance, ξ_{eff}. (B) The separation of the fringes varies accordingly.

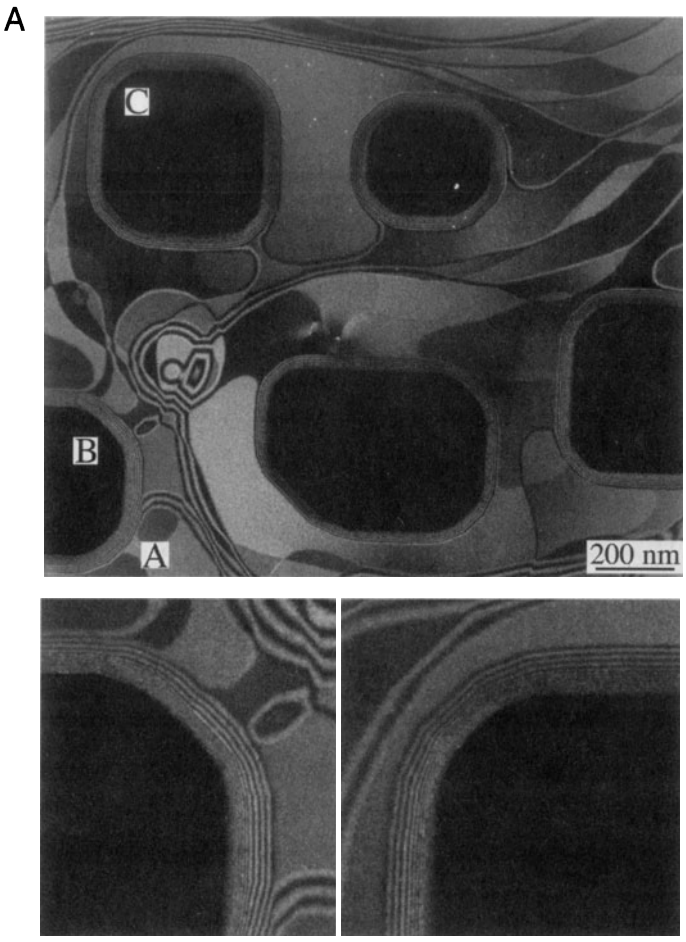

Figure 26.7. (A) WB thickness fringes from annealed MgO. (B,C) Higher magnification of regions B and C. Compare to Figure 23.3.

Before heating, the specimen had been acid etched, which caused the holes seen in this image (they're black because we're in DF). The specimen shows inclined steps which curve across the surface. Where we see wide uniform gray regions the surface is atomically flat. At A there is a large inclined step which runs into the hole B. Notice how the number of fringes around the hole increases at A. Around the holes (Figures 26.7B and C) we see much more closely spaced fringes because the thickness changes more quickly here. Now if we look at the edge of any hole such as C, we see that the spacing of the fringes has one value away from the hole but another, smaller value close to the hole. What we find is that the inclined surface facets on different planes with each facet becoming steeper closer to the hole. This topology is a result of the way the specimen has been prepared and would not normally be found, say, in electrochemically polished specimens, but it does illustrate the possibility of "profiling" using thickness fringes.

26.5. IMAGING STRAIN FIELDS

The principle of the technique is very simple. When the area of your specimen in which the defect of interest lies is oriented away from the Bragg position, the reflecting planes may be bent back into the reflecting position close to the defect. The region over which this occurs is very small because the strain has to be quite large to cause this bending. For the (220) planes in Cu (which fixes the plane spacing, d), the planes must rotate through an angle of ~2° to change $\mathbf{s}$ locally from 0.2 nm^{-1} to zero.

> The intensity of the reflection that we see in the DP is still small even though a relatively intense peak may occur in the image close to the defect core because the DP averages over a large area.

When you look at dislocations in the WB image, you see bright lines on a dark background. Let's compare the WB image to a BF image of the same defect in Figure 26.8. You can see that the WBDF image is much narrower;

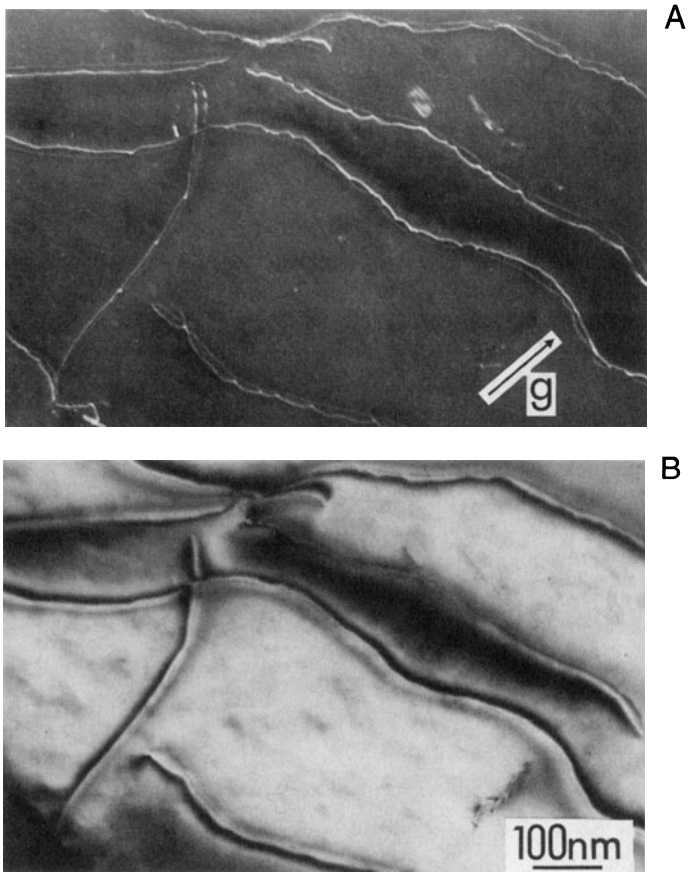

Figure 26.8. A comparison of dislocation images in a Cu alloy formed using (A) WB and (B) strong-beam ($\mathbf{s}_g > 0$) conditions.

you could make the comparison look even better if you make **s** very close to zero in the BF image.

We'll keep our discussion of dislocations brief but draw your attention to a few particular points:

- In the WB technique, most of the specimen is tilted so that **s** is large; the lattice planes in most of the specimen are then rotated away from the Bragg condition. However, as you can see in Figure 26.9, near the core of the dislocation the planes are locally bent back into the Bragg condition.
- This bending is only large close to the core of the dislocation (i.e., at the same depth from the surface).
- The peak you see in the WB image is always displaced to one side of the dislocation core. If you reverse the sign of **g**, the peak moves to the other side of the core. If you reverse the Burgers vector, **b** (rotate the diagram in Figure 26.9 through 180°), but keep **g** the same, the peak again moves to the other side.

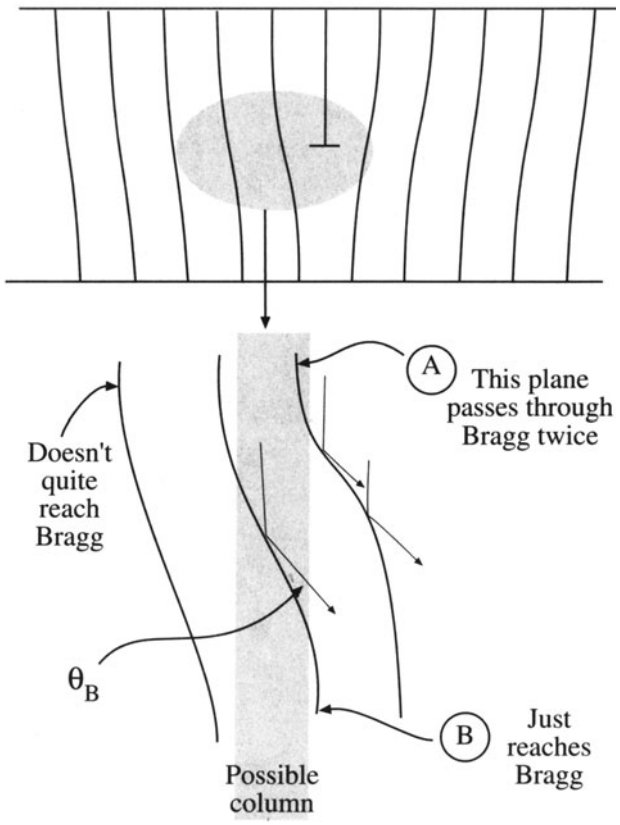

Figure 26.9. WB images of defects show high intensity close to the defect because only there are the diffracting planes bent back into the Bragg condition. This illustration is for an edge dislocation.

- If you increase **s** in the crystal, then the planes must bend more to satisfy the Bragg condition, which means the peak will move closer to the dislocation core.
- When we say "position of the peak," we are always talking about a projected position where the projection is along $\mathbf{k}_D$.
- There will be some situations where the strain is not large enough to compensate for the **s** you have chosen. Then you will only see poor contrast in the image.

26.6. PREDICTING DISLOCATION PEAK POSITIONS

There are three ways to calculate the contrast in a WB image. Since each teaches us something new, we'll go through them in turn.

Method 1: The WB Criterion states that the largest value of ϕ_g in the WB image occurs when s_R, which we derived in equation 25.7, is zero. We can express this result as

$$s_R = s_g + \mathbf{g} \cdot \frac{d\mathbf{R}}{dz} = 0 \qquad [26.6]$$

Equation 26.6 tells us that if the effective value of s (i.e., s_{eff}) is zero, even though s_g is not zero, then the direct beam and the diffracted beam, **g**, are strongly coupled. In this situation the strain field effectively rotates the lattice planes into the Bragg-reflecting position (Hirsch *et al.* 1977). Therefore, the crystal can be oriented so that ϕ_g is small for all columns except those near the dislocation core, where it can attain a considerable magnitude due to the strong coupling with the transmitted beam as it passes through the region close to the core of the dislocation where s_{eff} is zero. This increased amplitude is then retained below the core when the coupling between the two beams is decreased again. The intensity is expected to be largest for that column where s_{eff} remains closest to zero over the longest length, and this occurs for the column where there is an inflection in the curve of **R** versus z (Cockayne *et al.* 1969, Cockayne 1972 and 1981). Therefore, the position of the WB peak should occur when equation 26.6 is satisfied at a turning point of $\mathbf{g}\cdot(d\mathbf{R}/dz)$.

Method 2: The Kinematical Integral. An alternative criterion for defining the position of the WB peak was derived by Cockayne (1972). In the approximation where only two beams are considered and **s** is sufficiently large, Cockayne showed that the maximum scattering from the transmitted to the diffracted beam occurs where the kinematical integral, defined as

$$\int_{\text{column}} e^{\left\{-2\pi i\left(s_g z + \mathbf{g}\cdot\mathbf{R}\right)\right\}} dz \qquad [26.7]$$

is maximized. This maximum, in general, occurs for a column which is closer to the dislocation core than predicted by *Method 1*. The reason for this difference is interesting: because the planes are bent, the reciprocal lattice point is, on average, nearer to the Ewald sphere. Therefore, the integral has a larger value over the length of the column.

Without doing all the math, we can illustrate how these two approaches are related. What we want to do is determine when ϕ_g is large, but still kinematical (i.e., $\mathbf{s}$ is large); we want to maximize the kinematical integral in equation 26.7. We can do this using the stationary-phase method described by Stobbs (1975). We write the integral as

$$\int_0^t \exp\left(-2\pi i\left[\frac{z^2}{2}\cdot\frac{d^2}{dz^2}(\mathbf{g}\cdot\mathbf{R}) - \frac{z^3}{3}\cdot\frac{d^3}{dz^3}(\mathbf{g}\cdot\mathbf{R})\right]\right)dz \qquad [26.8]$$

where we have set $s + d/dz\ (\mathbf{g}\cdot\mathbf{R}) = 0$. If we also set $d^2/dz^2(\mathbf{g}\cdot\mathbf{R}) = 0$ (at the inflection), we go further to ensuring that the term in the square brackets is zero. This condition is what we guessed for the first method of defining the WB criterion.

Method 3: Compute the Contrast. Now that personal computers are widely available, we can calculate the position of the WB peak and graph the results. What we then find is that the WB peak actually lies between the two values predicted by the two criteria deduced using the first two methods. We also find, using the computer, that the position and width of the image peak are affected by any strongly excited diffracted beams so these *must* be avoided. A practical point is that the computer sometimes gives a rather pessimistic view of the variability in the peak position, so we have to weight the results carefully. Remember that the important advantages of this approach are that we can include the effects of the other diffracted beams which are always present, and we can take account of other variables, such as the convergence of the beam.

In the kinematical approximation, the half-width, Δx, of the image of an undissociated screw dislocation with $|\mathbf{g}\cdot\mathbf{b}| = 2$ is given approximately by the relation derived by Hirsch *et al.* (1960)

$$\Delta x = \frac{1}{\pi s_{\text{eff}}} \simeq \frac{\xi_{\text{eff}}}{3} \qquad [26.9]$$

This expression is a very useful rule of thumb. You will realize that this WB image width is special for three reasons, which arise because it doesn't depend on ξ_g. So, once $\mathbf{s}$ is fixed in a WB image, we can make several surprising statements regarding the width of the dislocation peak:

- It does not depend on the material.
- It does not depend on the reflection.
- It does not depend on the kV.

Take the example of the 220 reflection in Cu at 100 kV: ξ_g is 42 nm, and the width Δx is 14 nm. So, even if equation 26.9 is slightly wrong, the image width is greatly reduced in WB. If we make $s_g = 0.2$ nm^{-1}, then the half-width is 1.7 nm.

Computed many-beam images confirm that dislocations in other orientations give rise to similar narrow peaks when this value of s_g is used. A series of peak profiles for different values of t is shown in Figure 26.10. Notice that although the intensity of the peak may be only

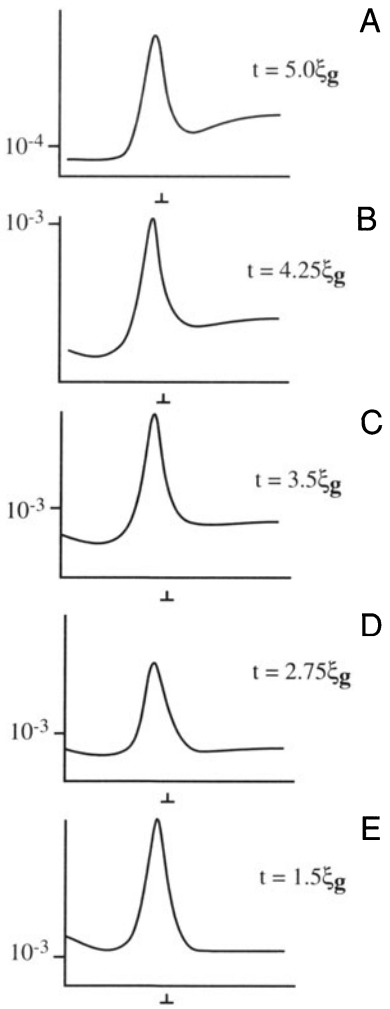

Figure 26.10. Examples of computer-calculated intensity peaks in WB images of an edge dislocation in Cu for different values of t. The intensity is relative to unit incident beam intensity.

about 0.1% of the incident beam, it is still much higher than the background.

For WB microscopy, $s_g = 0.2$ nm^{-1} is always a useful guide; it satisfies the requirements that the image should have a narrow width and show a high contrast between the defect and background regions.

Equation 26.9 indicates that as we increase the value of s, the half-width of the image peak decreases. However, a maximum is imposed on s by the fact that the intensity of the diffracted beam varies as s^{-2}. If we make s much larger, the contrast of the image therefore becomes too small to be of practical use.

The basic requirements governing the value of s which you must use for quantitative imaging are:

- $s \geq 2 \times 10^{-2}$ Å^{-1} to give sufficiently narrow peaks for fine detail to be studied.
- $s \leq 3 \times 10^{-2}$ Å^{-1} because the intensity varies as s^{-2} in the kinematical limit.
- $s\xi_g \geq 5$ to give sufficient contrast in the WB image.

If you use the **g**(3**g**) condition for Cu with **g** = 220 and 100-keV electrons, then the value of $\mathbf{s}_g$ will be 0.238 nm^{-1}.

26.7. PHASOR DIAGRAMS

We sometimes find it useful to demonstrate the depth dependence of the contrast in the WB image using phasor, or amplitude-phase, diagrams which we introduced in Chapter 2. You can generally use such diagrams whenever the kinematical approximation holds; they are equivalent to a graphical integration of the two-beam equations for the case where **s** is large. In fact, many of the early calculations of defect contrast were made using this approach before computers became widely available. We recommend that you glance at the original paper by Hirsch *et al.* (1960).

The basic idea is shown in Figure 26.11. We simply add all the $d\phi_g$ increments to ϕ_g. In doing so, we take account of the phase changes which occur as the beam passes through the crystal. Remember that in this approximation, no electrons leave the **g** beam! If the crystal is perfect and our increments are sufficiently small, we will produce a smooth circle.

The circumference of this circle is ξ_{eff} as we require for the depth periodicity, and the radius is $\xi_{eff}/2\pi$ or $(2\pi s_{eff})^{-1}$. Notice that as we increase **s**, we decrease ξ_{eff} and the circle becomes smaller. Thus we move around the circle more quickly if **s** is large. In other words, our effective extinction distance is reduced, as we knew from Chapter 13.

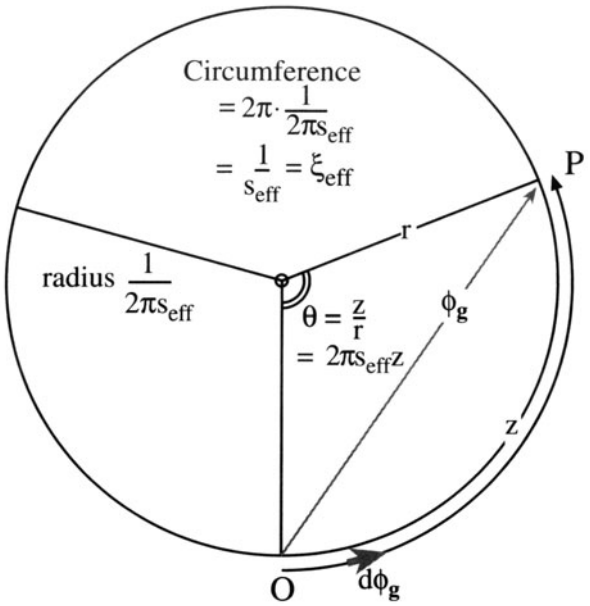

Figure 26.11. A phasor diagram for the WB case. The distance z is the arc OP measured around the circumference and the radius of the circle is $(2\pi s_{eff})^{-1}$.

If the diffracted beam passes through a stacking fault, it will experience an extra phase shift given by $2\pi\mathbf{g}\cdot\mathbf{R}$. Using the familiar example for an fcc crystal, we take an example where $\mathbf{R} = \frac{1}{3}[11\bar{1}]$ and $\mathbf{g} = (20\bar{2})$, which gives $\alpha = 2\pi/3 = 120°$ (modulo 2π). The abrupt phase change is shown at P_3 in Figure 26.12. Now, the value of ϕ_g (P_1P_2) can be much larger than in a perfect crystal. The locus of ϕ_g still travels round the first circle until it meets the

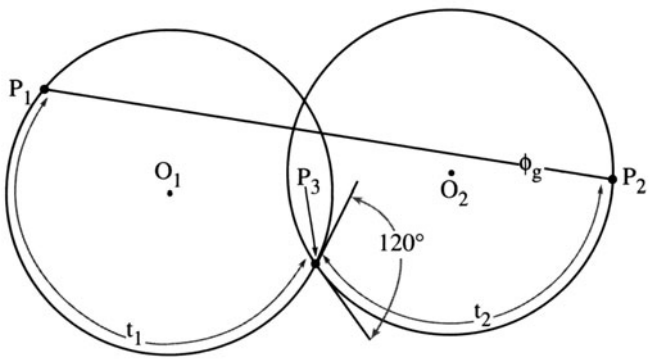

Figure 26.12. A phasor diagram used to explain the WB contrast from a SF at depth t_1 in a foil of thickness $t_1 + t_2$. P_1 is the top and P_2 the bottom of the foil. Here, the phase change at the SF (P_3) is 120°.

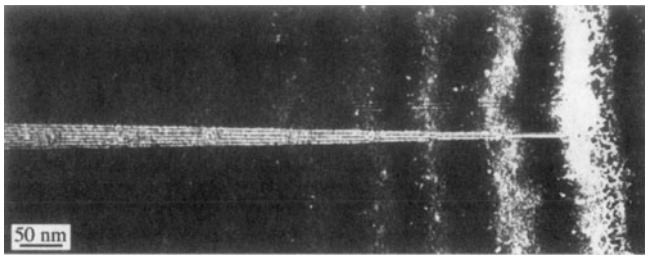

Figure 26.13. Illustration of thickness fringes in an experimental image of two inclined SFs in a wedge specimen of spinel. The thickness fringes from the wedge and from the inclined SF can be clearly seen and counted. The second SF shows little contrast because it has a different **R** value.

planar fault at $z = n\xi_{eff} + t_1$, where z and t_1 are measured parallel to $\mathbf{k_D}$. It then moves onto the second circle until it reaches $z = t$. You can readily see that if we keep the depth of the fault, t_1, fixed, we then see depth fringes which vary with periodicity ξ_{eff} as we vary the total thickness, t. (The value of α is still 120°.) The situation is a little more difficult to envision if we keep t fixed but vary t_1, but the principle is the same. Images of WB fringes at inclined SFs are illustrated in Figure 26.13. The thickness fringes of the wedge specimen and those from the inclined stacking fault can both be clearly seen and counted. Notice that the number of bright fringes on the planar defect really does increase by one for every increment ξ_{eff} in the thickness of the wedge and you don't need to know **R**.

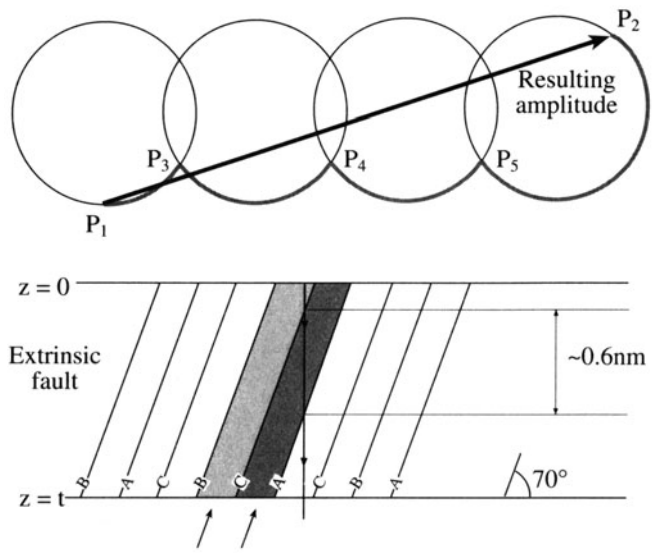

Figure 26.14. Phasor diagram for a series of overlapping planar defects at P_3, P_4, and P_5. For a 111 foil normal, the inclined $11\bar{1}$ planes lie at 70° to the surface so that the spacing between adjacent planes in the direction of the beam is 0.627 nm. Compare with Figure 26.12.

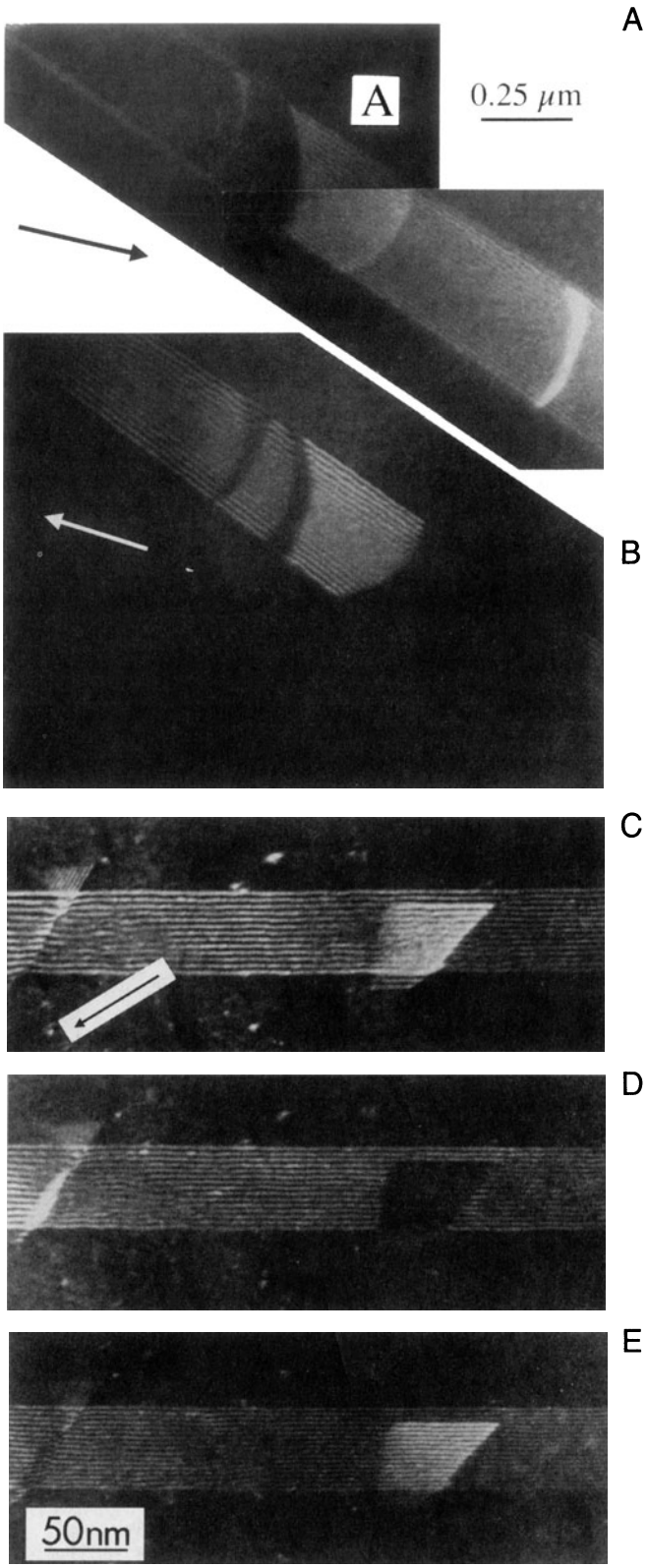

Figure 26.15. (A,B) Overlapping SFs imaged in WBDF conditions for ±**g**. Many more fringes occur than in the BF image in Figure 24.5. Fringes occur at A where the BF image showed no contrast. (C–E) Changes in fringe spacing and intensity in the overlapping region as **s** increases.

You can imagine applying this analysis to the situation where you have several overlapping planar faults, as shown in Figure 26.14. ϕ_g (P_1P_2) can become very large (does our approximation of unit incident intensity still hold?). This situation does occur in practice, as shown in Figure 26.15. Here we have several overlapping faults. The bright ones are bright even when ϕ_g reaches its minimum, as you would expect from Figure 26.14. If you compare the WB image with its strong-beam counterpart in Figure 24.5, you will notice that there is much more detail in the WB image; as we saw in Chapter 24, overlapping faults on nearly adjacent planes can essentially give no contrast in the BF image. You can easily check such effects in WB by adjusting **s** as in Figures 26.15C–E. It's interesting to realize that this effect can occur even when two intrinsic SFs lie on adjacent planes to give the extrinsic SF (Föll *et al.* 1980, Wilson and Cockayne 1985). This approach can be used to image other planar defects, such as the {112} twin boundary which can have a significant thickness (Carter *et al.* 1995). The key factor is that, under WB conditions, ξ_{eff} can become comparable to the distance that the beam travels between encountering successive planes of atoms, particularly when the interface is quite steeply inclined relative to the beam.

We can also use a phasor diagram to describe the contrast from a dislocation, but now the phase change occurs over a range of thickness rather than at a particular value. As illustrated in Figure 26.16, the phase can either add or subtract depending on the sign of $\mathbf{g}\cdot\mathbf{R}$. When the phase changes quickly with a change in t, as at the center of Figure 26.16, it means that we are strongly coupling the incident and diffracted beams.

We'll summarize our discussion of phasor diagrams with two points:

- They should only be used when the kinematical approximation holds.
- They then give us a graphical method for understanding the variation of ϕ_g with thickness, especially when crystal defects are present.

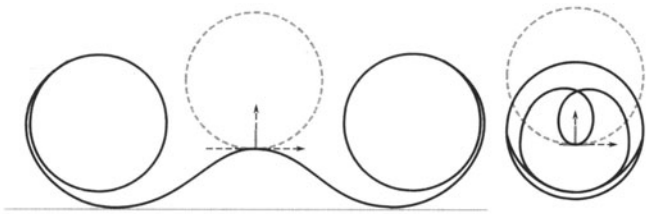

Figure 26.16. Phasor diagrams for a dislocation for ±**g**. The phase change is not abrupt but rather occurs over an extended distance along the column. In the left diagram the phase change is the direction shown in Figure 26.12, but in the right diagram the phase change has the opposite sign.

26.8. WEAK-BEAM IMAGES OF DISSOCIATED DISLOCATIONS

Although the study of dislocations is a very specialized topic, it beautifully illustrates the potential of the WB technique. Dissociated dislocations are common in face-centered-cubic (fcc) materials (including Si) and ordered intermetallics such as Ni_3Al. The geometry of a dissociated dislocation in Cu is summarized in Figure 26.17. We gave some general references on the theory of dislocations in Chapter 25.

Since the computed many-beam images show that the position of the dislocation image lies close to the position predicted by the WB criterion, this criterion is used in practice because it allows us to deduce an equation for the position of the image. We can thus directly relate the separation of Shockley partials, for example, to the measured separation of the two peaks observed in $|\mathbf{g}\cdot\mathbf{b}_T| = 2$ images of dissociated dislocations. Hence we can estimate the stacking-fault energy (SFE) of semiconductors and several fcc metals. (See Carter 1984 for a review of dissociated dislocations and Geerthsen and Carter 1993 for a comparison of WB and HRTEM.) In order to interpret WB images of extended dislocation configurations, we need to know how the position of the image peak is related to the position of the dislocation core. This information is essential whenever we use the WB technique to collect *quantitative*

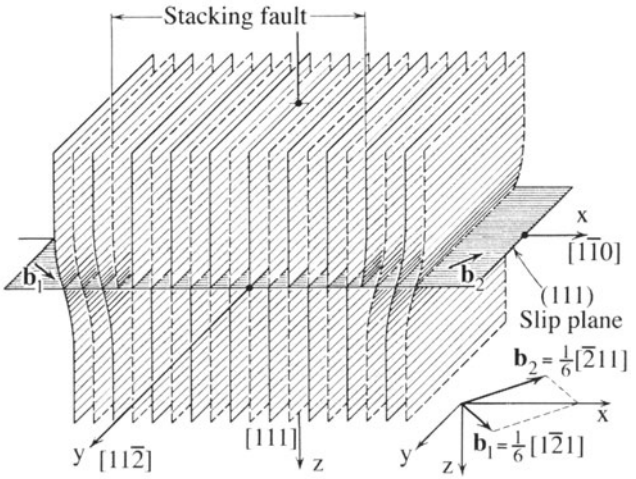

Figure 26.17. The geometry of a perfect dislocation in Cu. The perfect dislocation separates into two Shockley partial dislocations with Burgers vectors $\mathbf{b}_1$ and $\mathbf{b}_2$ separated by a SF on a {111} plane.

data. We will now answer two questions for quantitative WB analysis:

- What factors determine the position of the WB peak?
- What methods are used to determine the Burgers vectors of the dislocations?

When the WB conditions are satisfied, dissociated dislocations can be imaged in a {220} reflection for which $|\mathbf{g}\cdot\mathbf{b}_T| = 2$, so that each partial dislocation gives rise to an intensity peak having a half-width of 1 to 1.5 nm. The separation of the partials can be deduced to within ±0.7 nm providing that the peak separation is greater than ~2.5 nm. For many materials, we need to use anisotropic elasticity theory to relate the atomic displacements to the image, so the computer becomes essential.

Why not just use HRTEM since, as we'll see in Chapter 28, HRTEM can give detail down to below 0.2 nm, whereas WB is often limited to ~1 nm? If you want to interpret an HRTEM image the defect must be *absolutely straight*, parallel to the beam, and located in a very thin region of the specimen. The segment of dislocation studied by HRTEM will thus be no longer than 20 nm and less than 10 nm for the highest resolution. In a WB image the defect can be micrometers long and, in a relatively thick foil, it can even change direction. If you look back at Figure 26.8 you'll see pairs of lines which correspond to partial dislocations in the WB image. You can see other features, such as constrictions. The strong-beam image may also show two or more lines for a particular dislocation but, as we saw in Chapter 25, these lines are not related to the detailed structure of the dislocation but rather to n in the equation $\mathbf{g}\cdot\mathbf{b} = n$.

Ideally, for quantitative analysis, you should choose long, nearly straight dislocations. As shown in Figure 26.17, the two Shockley partial dislocations lie in the (111) plane of the foil. The Burgers vectors of the total and partial dislocations can be determined by imaging the dislocation in the WB mode using the $\{2\bar{2}0\}$ reflections. A sharp peak is found for a partial dislocation with $|\mathbf{g}\cdot\mathbf{b}_p| = 1$, and either no peak or a diffuse one (arising from the anisotropy of the lattice) if the partial dislocation has $|\mathbf{g}\cdot\mathbf{b}_p| = 0$. When $|\mathbf{g}\cdot\mathbf{b}_T| = 2$, the diffraction vector $\mathbf{g}$ and the Burgers vector $\mathbf{b}_T$ are parallel and, in the image of a dissociated dislocation, two sharp peaks are formed, one corresponding to each of the partial dislocations (both now have $|\mathbf{g}\cdot\mathbf{b}_p| = 1$).

One of the peaks is on average more intense than the other; the order reverses when $\bar{\mathbf{g}}(3\bar{\mathbf{g}})$ is used instead of $\mathbf{g}(3\mathbf{g})$.

We can explain this difference in intensity if one peak (the weaker) arises from the region between the partial dislocations and the other from outside the dissociated dislocation. This effect cannot occur in $|\mathbf{g}\cdot\mathbf{b}_T| = 1$ images, when $|\mathbf{g}\cdot\mathbf{b}_p| = 1$ for one partial and $|\mathbf{g}\cdot\mathbf{b}_p| = 0$ for the other, and it can be used to identify the reflection for which $|\mathbf{g}\cdot\mathbf{b}| = 2$. Confirmation of the Burgers vector is always obtained using the BF mode, observing characteristic $|\mathbf{g}\cdot\mathbf{b}_T| = 2$ or $|\mathbf{g}\cdot\mathbf{b}_T| = 0$ images.

In a WB image with $|\mathbf{g}\cdot\mathbf{b}_T| = 2$, each of the partial dislocations will generally give rise to a peak in the image which is close to the dislocation core (Cockayne *et al.* 1969). You can calculate the approximate positions of these peaks using the criterion from equation 26.6. Then, you can relate the separation of the peaks in the image to the separation Δ of the partial dislocations.

We can write the displacement, using isotropic elasticity theory, as the sum of the displacements due to the individual partial dislocations. If the Burgers vector of a straight, mixed dislocation lies in the (111) plane parallel to the surface of a foil, then at a distance x from the dislocation core

$$-s_g = \frac{|\mathbf{g}|}{2\pi}\left[\left(|\mathbf{b}_1| + \frac{|\mathbf{b}_{1e}|}{2(1-\nu)}\right)\frac{1}{x} + \left(|\mathbf{b}_2| + \frac{|\mathbf{b}_{2e}|}{2(1-\nu)}\right)\frac{1}{x-\Delta}\right] \qquad [26.10]$$

Here x defines an axis perpendicular to both the dislocation line and the beam direction, and e refers to the edge component of the Burgers vectors of the partial dislocations, 1 and 2. This relation is particularly simple because, for the geometry we have chosen, the term $\mathbf{g}\cdot\mathbf{b}\times\mathbf{u}$ is zero. Using the notation

$$a = -s_g\left[\frac{|\mathbf{g}|}{2\pi}\left(|\mathbf{b}_1| + \frac{|\mathbf{b}_{1e}|}{2(1-\nu)}\right)\right]^{-1} \qquad [26.11]$$

and

$$b = -s_g\left[\frac{|\mathbf{g}|}{2\pi}\left(|\mathbf{b}_2| + \frac{|\mathbf{b}_{2e}|}{2(1-\nu)}\right)\right]^{-1} \qquad [26.12]$$

equation 26.10 reduces to

$$1 = \frac{1}{ax} + \frac{1}{b(x-\Delta)} \qquad [26.13]$$

which has two solutions, x_+ and x_-, given by

$$x_\pm = \frac{ab\Delta + a + b \pm \left[(ab\Delta + a + b)^2 - 4ab^2\Delta\right]^{\frac{1}{2}}}{2ab} \qquad [26.14]$$

These values of x define the positions of the peaks in the image. The separation between these peaks is then given by

$$\Delta_{obs} = \left[\Delta^2 + \frac{(a+b)^2}{a^2b^2} + \frac{2(a+b)\Delta}{ab} - \frac{4\Delta}{a}\right]^{\frac{1}{2}} \qquad [26.15]$$

We can rearrange this equation to make it appear more symmetric in a and b. Of course, it will not be symmetric because the peak is always located on one side of the dislocation.

$$\Delta_{obs} = \left[\left(\Delta + \frac{1}{b} - \frac{1}{a}\right)^2 + \frac{4}{ab}\right]^{\frac{1}{2}} \qquad [26.16]$$

Computed images confirm that this relation is accurate for $\Delta_{obs} > 2.5$ nm, to within ±0.7 nm (Cockayne 1972). This uncertainty is due to the variation of the peak position with the depth of the dislocation in the foil and the foil thickness. A small uncertainty arises when you have not determined the actual direction of $\mathbf{b}_T$, i.e., whether it is in the direction of $\mathbf{g}$ or $\bar{\mathbf{g}}$. Stobbs and Sworn (1971) have found, using anisotropic elasticity theory, that the relation (equation 26.16) subject to the ±0.7 nm uncertainty is still a good approximation.

As a simple exercise, consider the WB images of a dissociated screw dislocation and a dissociated edge dislocation. You should pay particular attention to "a" and "b," because in one case $\mathbf{b}_{1e}$ and $\mathbf{b}_{2e}$ have the same sign, while in the other the sign is opposite. Does the image always have the same width when you reverse $\mathbf{g}$?

Example 1. Even if you never want to calculate the actual separation of two dislocations from observations of two peaks, you can learn new ideas about dislocations from such images. Figure 26.18 is a famous set of images showing a dislocation in Si which is constricted along part of its length and dissociated along the rest. Even if you don't know the precise details of the dislocation structure, you know that it can adopt two variants; the rest of the task is modeling the defect.

Example 2. The WB image of the node pair in Figure 26.19A tells you very quickly that the two nodes are different; if we form images using other $\mathbf{g}$ vectors, (B–D) we find that one of the partial dislocations is out of contrast in the image. The extended node contains the same type of intrinsic stacking fault that is present in the dissociated dislocation; $\mathbf{g}\cdot\mathbf{R}$ is zero in this image for the stacking fault. The other node is constricted, within the detectability of the WB technique. Comparison with the BF images in Figure 25.8 is instructive.

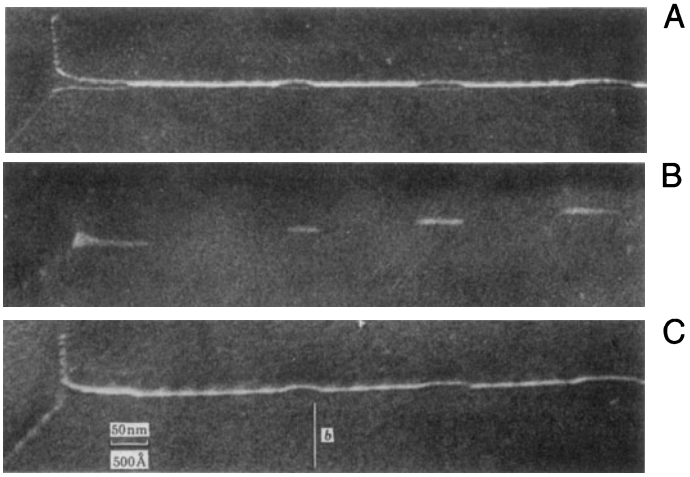

Figure 26.18. WB image of a dislocation in Si which has both dissociated and constricted segments: (A) $\mathbf{g}\cdot\mathbf{b} = 2$; both partial dislocations are visible. (B) $\mathbf{g}\cdot\mathbf{b}_T = 0$ showing SF contrast. (C) $\mathbf{g}\cdot\mathbf{b} = 1$; only one partial dislocation is visible.

Example 3. We mentioned that the peak moves to the other side of the dislocation if we reverse $\mathbf{b}$. This is exactly what happens for a dislocation dipole as you can see in Figure 26.20. This is a complicated figure except that you can use it not only to see the inside–outside contrast in WB images of dislocation dipoles but also as an exercise in $\mathbf{g}\cdot\mathbf{b}$ analysis. A dislocation dipole is a pair of dislocations identical in every way, apart from the sign of the Burgers vector. If we now reverse $\mathbf{g}$, then both peaks move to the other side of their respective dislocations. This change in contrast is referred to as inside–outside contrast and is commonly seen on dislocation loops, which are themselves closely related to these dipoles (just more "equiaxed"). The images shown in Figures 26.20B,C illustrate the dramatic change in contrast which you can see on reversing $\mathbf{g}$. Some of the dipoles completely disappear in (A–C) because they are a special form of defect known as a faulted dipole. Such dipoles usually give very low contrast in strong-beam BF images because the dislocations are always very close together so that their strain fields overlap, and the lattice is thus only distorted over very small distances. When we use the WB technique, we are probing the structure on these very small dimensions and the contrast can be high. Again, compare with the BF image in Figure 25.13.

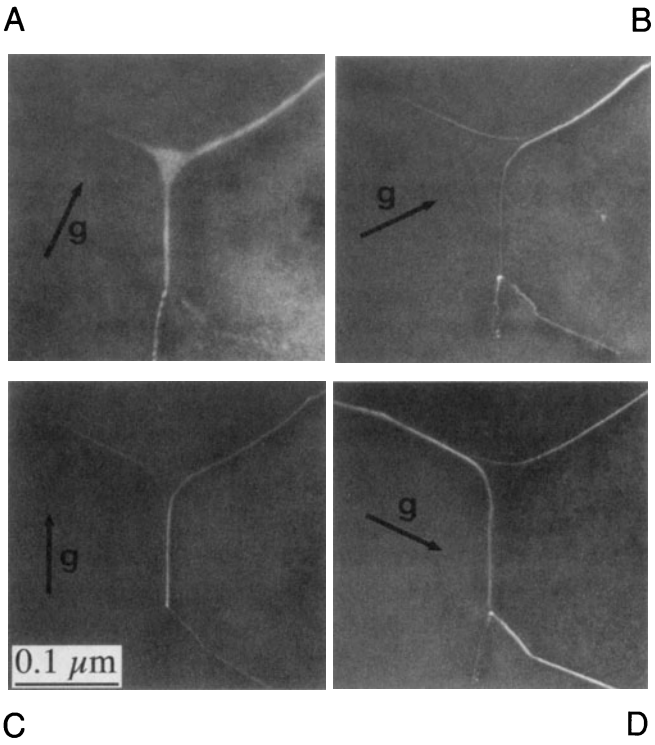

Figure 26.19. WB images of a pair of dislocation nodes formed by the dissociation of interacting dislocations lying on a {111} plane in a Cu alloy. The SF is imaged in (A) and, imaging with different reflections (B–D), the partial dislocations are out of contrast when $\mathbf{g}\cdot\mathbf{b} = 0$. Compare with the BF image in Figure 25.8 and note the difference in magnification.

Examples 4 and 5. The WB technique allows us to see features which would be hidden if we used strong-beam imaging. Figure 26.21 gives an example where an inclined SF is cutting through several dissociated dislocations. The interaction of the two defects would be masked by the SF fringes in the strong-beam image but is clearly visible in this WB image. Seeing small particles close to dislocations is difficult in strong-beam imaging. Although not easy in WB, Figure 26.22 does illustrate that it can be done. These images show, for example, that the behavior of the dissociated dislocation is different on each side of the particle (see also Figure 26.23), and again stress the advantage of WB over BF imaging.

Example 6. We noted in Section 25.8 that the surface of the specimen can affect the geometry of the defects we are examining. In general, the specimen needs to be thinner for WB imaging than for strong-beam imaging. Therefore, surface effects can be even more important. Figure 26.23 shows an example where this effect is particularly clear. Dislocations which were uniformly separated in the bulk material now appear wedge-shaped: the effects of the two surfaces are different in this case (Hazzledine *et al.* 1975).

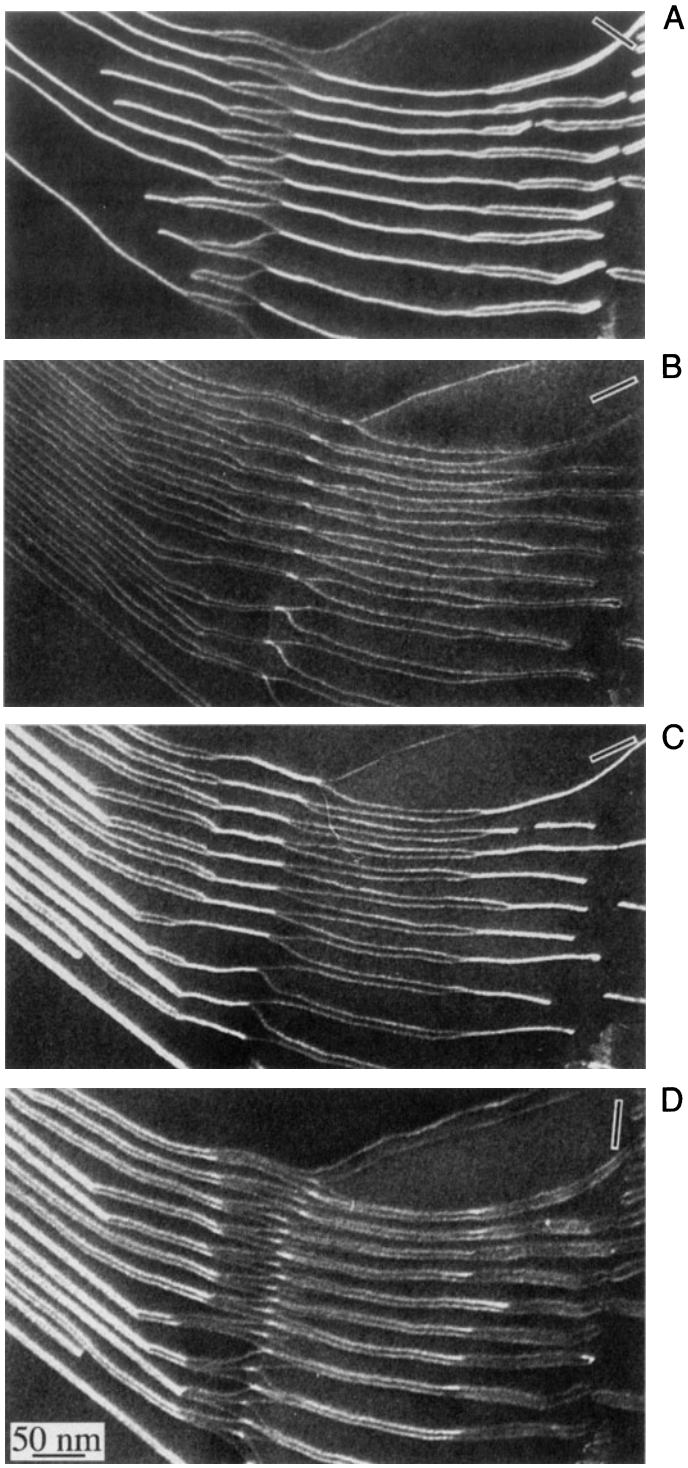

Figure 26.20. Four WBDF images showing an array of dislocation dipoles in a Cu alloy having a low stacking-fault energy. The reflections are all 220-type and the dislocations all lie on (111) planes which are nearly parallel to the surface of the specimen. All the dislocations are dissociated. All the Shockley partial dislocations are in contrast in (D) while half are out of contrast in (A–C). Notice that the narrower images are brighter than the wider ones: the strain is large in between the dislocations but decreases rapidly outside the dipole since the total Burgers vector of a dipole is zero.

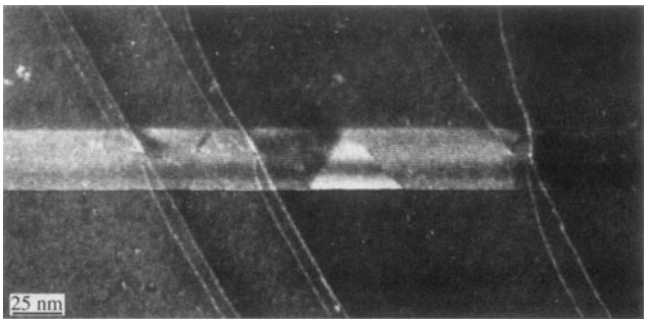

Figure 26.21. WB image of an inclined SF cutting through a series of dissociated dislocations lying parallel to the surface of the Cu-alloy specimen.

26.9. OTHER THOUGHTS

26.9.A. Thinking of Weak-Beam Diffraction as a Coupled Pendulum

We can illustrate the principle which underlies the increase in intensity in the WB image close to a dislocation using the mechanical analog of a coupled pendulum. A diagram is shown in Figure 26.24. The two pendula are connected (coupled) by a third string. If we start the left pendulum swinging but hold the connecting string, the right-hand pendulum remains stationary. Now release the connecting string. You will see that the right-hand pendulum now begins to swing. If we let the process continue, eventually the right-hand pendulum is swinging as much as the original one did, but the original one is stationary: this is the strong-beam analog! All the kinetic energy has been transferred from one pendulum to the other. Given more time, we will achieve the original condition. Now repeat the exercise, but hold the connecting string again after the right-hand pendulum has begun to swing; you will notice that both pendula continue to swing, each with a constant amplitude. The role of the connecting string is to couple the two pendula (beams) so that we transfer energy from one beam to the other. In WB TEM, the defect acts as the connecting string. The two beams are only coupled over a short length as they travel past the defect. We can plot this amplitude (or intensity); try this as an exercise.

26.9.B. Bloch Waves

We discussed Bloch waves in Chapter 14. The difficulty in applying Bloch-wave analysis to the WB situation is that we are usually interested in defects. However, we can make some basic comments. For the reflection **g** to give a WB image, $|\phi_g|$ must be much smaller than unity in the regions of perfect crystal but, in strained regions, a change

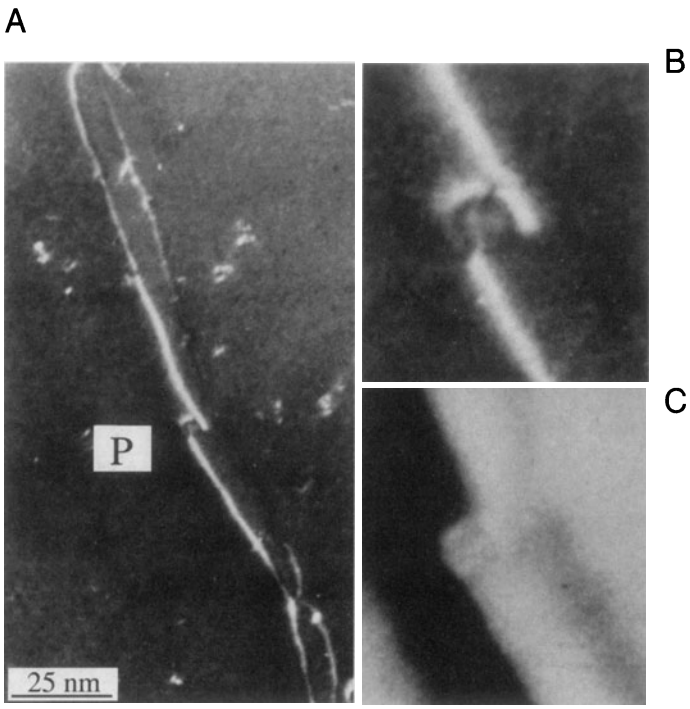

Figure 26.22. (A) WB image of a dissociated dislocation interacting with a particle (P) in a Cu alloy. (B) and (C) are enlargements of the WB and corresponding BF images, respectively.

$\Delta\psi^{(j)}$ in the amplitude of the Bloch wave j can give rise to a change $\Delta\phi_g$. Cockayne has shown that the appreciable contrast which can then be present in the WB image is due, in the two-beam approximation, to the interband scattering from Bloch wave 1 to Bloch wave 2. In the general case, the scattering is from the branch of the dispersion surface with the largest $\psi^{(j)}$ to those branches with the largest $C_g^{(j)}$, i.e., from the Bloch wave with the largest amplitude to the one which is most strongly excited. The dispersion surface for the **g**(3**g**) diffraction geometry is shown in Figure 26.25. It's an instructive exercise to reread this paragraph thinking how each statement relates to this figure, and to consider other diffraction geometries, e.g., **0**(2**g**).

Figure 26.23. WB image showing the dissociation of a group of dislocations which are inclined to the foil surface to give wedge-shaped SFs. The shape of the SFs is caused by surface stresses.

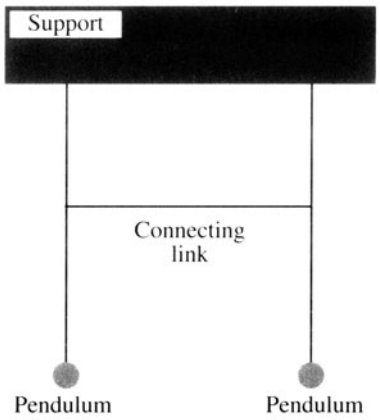

Figure 26.24. The coupled pendulum.

The Bloch-wave analysis of the problem leads to two further points which simplify the interpretation of WB images:

- The diffraction conditions should be such that only one interband scattering process is important.
- In the two-beam approximation, in order for the image peaks to show sufficient contrast, it is generally found that w ($= s\xi_g$) is greater than ~5.

You can satisfy the first requirement by ensuring that no reflections are strongly excited. The second condition is usually already satisfied because of the more stringent requirement that **s** should be greater than 0.2 nm^{-1}. For example, for a $\{2\bar{2}0\}$ reflection in copper with 100-keV electrons, w is automatically greater than 8 since ξ_g is 42 nm.

The **g**(3.1**g**) condition may also be preferable to **g**($\bar{\mathbf{g}}$) on theoretical grounds if images are to be compared with computed profiles made using the column approximation, i.e., it simplifies your interpretation. The basis for this suggestion is that the region of the dispersion surface from which the scattering occurs is flatter for the **g**(3.1**g**) diffraction geometry than for the **g**($\bar{\mathbf{g}}$) case.

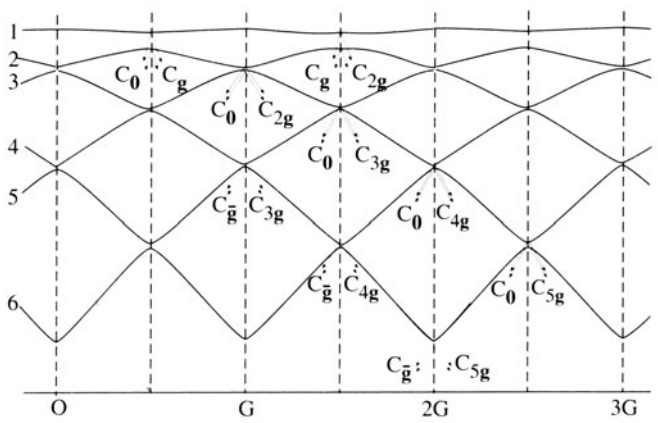

Figure 26.25. Dispersion surface construction which is used to describe the **g**(3**g**) geometry. The BZB is at 1.5G and tells you which reflections are strongly coupled; see Figure 15.9.

26.9.C. If Other Reflections Are Present

Several times in the previous discussion, we have said that no reflections should be strongly excited. Much of our thinking has been based on the two-beam approximation we introduced in Chapter 11. When you are using WB conditions, you must be even more careful. Consider the **g**,3**g** geometry shown in Figure 26.5. We form the WB image using reflection **g** so electrons are weakly scattered from the O beam into the G beam. However, once in the G beam, they can be strongly scattered into the 2G beam. We can picture this process by drawing the new Ewald sphere for the "new" incident beam, G; this sphere passes through 2G!

For the mathematically inclined, you can go back to the many-beam equations which we introduced briefly in Chapter 13. The coupling of beams **g** and **h** is determined by $(s_g - s_h)^{-1}$ and has an extinction distance given by ξ_{g-h}. If s_g and s_h are equal, then the coupling between these beams will be strong. Furthermore, the characteristic length for the coupling in this example will be ξ_{2g-g} or ξ_g, which is what you would have guessed from Figure 26.25.

26.9.D. The Future

Several new developments will change how we practice the WB technique. The main point here is that you should remember the principles because they will not change.

- Slow-scan CCD cameras give a very linear response and therefore make quantitative analysis of WB images possible. For this to happen, computer modeling of the defect and simulation of the image will be needed. We will return to this topic in Chapter 30.
- An FEG and energy-filtered imaging will allow us either to minimize the effect of variations in the energy or to form WB images using particular sections of the energy-loss spectrum. Then, we will need to extend the theory.
- Image processing and frame averaging should allow us to reduce the noise and again aid quantification.

Image simulation, as we described in Chapter 25, will allow us to be more quantitative in our interpretation of WB images.

CHAPTER SUMMARY

The basic idea of the WB technique is very simple: using a large value of **s** gives a small ξ_{eff} and hence a narrow image of most defects, since the width of a dislocation is related to $\xi_{eff}/3$. What you should remember is that the value of s for a particular diffraction condition **g**(n**g**) depends not only on n and **g**, but also the lattice parameter of the crystal and the wavelength of the electrons. You will see the "magic number" **s** = 0.2 nm^{-1} quoted often.

- Remember that this number gives a rule of thumb if you want to do quantitative analysis. It does not usually correspond to **g**(3**g**).
- Don't use the **g**(3**g**) condition without calculating the value of $\mathbf{s}_g$.
- The term **s**·**R** has been neglected in this analysis; we usually assume that the deformable-ion model from Section 24.13 is valid.

You can often get all the information you need with less effort using a somewhat smaller value of **s**. As always, the longer you take to perfect the image, the more likely you are to alter your specimen, especially the defect structure.

Finally, remember that the diffracted beam travels parallel to $\mathbf{k}_D$. Therefore, the image of any defect is also projected in this direction. Even though the Bragg angle is small, this means, for example, that the apparent separation of defects in the image may not be equal to their horizontal separation relative to their glide planes if the defects are located at different heights in the specimen. This projection error can vary, depending on the **g** and **s** used to form the image and the orientation of the specimen.

REFERENCES

Specific References

Carter, C.B. (1984) in *Dislocations–1984* (Eds. P. Veyssière, L. Kubin, and J. Castaing), p. 227, Editions du CNRS, Paris.

Carter, C.B., Mills, M.J., Medlin, D.L., and Angelo, J.E. (1995) 7th International Conference on Intergranular and Interphase Boundaries in Materials, Lisbon, Portugal.

Cockayne, D.J.H. (1972) *Z. für Naturforschung.* **27a**, 452.

Cockayne, D.J.H. (1981) *Ann. Rev. Mater. Sci.* **11**, 75.

Cockayne, D.J.H., Ray, I.L.F., and Whelan, M.J. (1969) *Phil. Mag.* **20**, 1265.

Föll, H., Carter, C.B., and Wilkens, M. (1980) *Phys. stat. sol. (A)* **58**, 393.

Geerthsen, D. and Carter, C.B. (1993) *Phys. stat. sol. (A)* **136**, 29.

Hazzledine, P.M., Karnthaler, H.P., and Wintner, E. (1975) *Phil. Mag.* **32**, 81.

Hirsch, P.B., Howie, A., Nicholson, R.B., Pashley, D.W., and Whelan, M.J. (1977) *Electron Microscopy of Thin Crystals,* 2nd edition, p. 164, Krieger, Huntington, New York.

Hirsch, P.B., Howie, A., and Whelan, M.J. (1960) *Proc. Roy. Soc. London* **A252**, 499.

Stobbs, W.M. (1975) in *Electron Microscopy in Materials Science,* Vol. **II** (Eds. U. Valdrè and E. Ruedl), p. 593, CEC, Brussels.

Stobbs, W.M. and Sworn, C.H. (1971) *Phil. Mag.* **24**, 1365.

Wilson, A.R. and Cockayne, D.J.H. (1985) *Phil. Mag.* **A51**, 341.